Article

The Sensitization of TiO$_2$ Thin Film by Ag Nanoparticles for the Improvement of Photocatalytic Efficiency

Vytautas Kavaliūnas *[ID], Paulius Čeplikas, Mantas Sriubas [ID] and Giedrius Laukaitis [ID]

Department of Physics, Kaunas University of Technology, Studentų St. 50, LT-51368 Kaunas, Lithuania;
paulius.ceplikas@ktu.edu (P.Č.); mantas.sriubas@ktu.lt (M.S.); giedrius.laukaitis@ktu.lt (G.L.)
* Correspondence: vytautas.kavaliunas@ktu.edu; Tel.: +370-681-74281

Abstract: The formation of Ag nanoparticles on the surface of TiO$_2$ (AgNP/TiO$_2$) to enhance photocatalytic efficiency was studied. The Ag nanoparticles (AgNP) size, form, and distribution dependence on the initial thickness of Ag thin films, annealing temperature, and time were analyzed. The optimal annealing temperature of 400 °C and annealing time of 60 min were chosen to form AgNP from the initial Ag thin films with a thickness of 5, 7.5, and 10 nm. The formation of AgNP was done on amorphous TiO$_2$ (a-TiO$_2$), which crystallized into the anatase phase after the annealing. The photocatalytic efficiency (k–degradation rate constant, D_{efi}–degradation efficiency) was evaluated by the photodegradation of Rhodamine B aqueous solution. The results suggested that the highest photocatalytic efficiency of Rhodamine B aqueous solution was reached where the average diameter (D_A) of AgNP was ~38 nm (k_{38} = 0.017 min^{-1}, D_{efi_38} = 63.5%), compared to 27 and 82 nm (k_{27} = 0.012 min^{-1}, D_{efi_27} = 51.2% and k_{82} = 0.011 min^{-1}, D_{efi_82} = 52.1%, respectively). The acquired results did not show clear correlation between the size and distribution of the AgNP on the TiO$_2$ surface and photocatalytic efficiency. Nevertheless, the results suggest that AgNP can enhance the photocatalytic efficiency of TiO$_2$ thin films (k_{TiO2} = 0.008 min^{-1}, D_{efi_TiO2} = 36.3%).

Keywords: titanium dioxide; silver nanoparticles; photocatalysis

1. Introduction

Hazardous organic contaminants from many sources, such as farms and factories, are frequently found in wastewaters and can cause environmental issues [1]. Therefore, photocatalytic degradation of various organic compounds in water has been investigated in the last few decades [2]. Various materials and their composites can decompose organic dyes in water: binary oxides (e.g., TiO$_2$, ZnO, ZrO$_2$), ternary oxides (e.g., SrTiO$_3$, LiTaO$_3$, NaTaO$_3$), solid solutions (e.g., βAgAl$_{1-x}$Ga$_x$O$_2$, (AgNbO$_3$)$_{1-x}$(NaNbO$_3$)$_x$), nanocomposite materials (e.g., TiO$_2$ nanorods, ZnO nanorods, TiO$_2$/ZnS) [3], or hybrid photocatalysts (Bi$_3$TaO$_7$/Ti$_3$C$_2$, Bi$_2$S$_3$/Bi$_2$O$_3$/Bi$_2$O$_2$CO$_3$) [4,5]. Of the many different photocatalysts, TiO$_2$ has been the most widely studied and used in many applications because of its strong oxidizing ability to decompose organic pollutants superhydrophilicity, chemical stability, long durability, nontoxicity, low cost, and transparency to visible light [6]. When TiO$_2$ or another photocatalyst absorbs a photon with energy equal to or higher than the band gap energy (E_g), electrons (e^-) jump from the valence band (*VB*) to the conduction band (*CB*), and an electron-hole (h^+) in the valence band forms. The e$^-$ and h^+ pair can recombine or move to the TiO$_2$ surface. These charge carriers react with the surface hydroxyl group or water and dissolved oxygen to produce hydroxyl (OH), peroxide (H$_2$O$_2$), and superoxide (O$_2^-$) radical anions. Later, the ·OH radicals react with the organic molecules to form CO$_2$, H$_2$O, NO$_3^-$, and NH$_4^+$ compounds [7]. However, the major drawbacks of TiO$_2$ as a photocatalyst are wide band gap, short recombination time of charge carriers in bulk or on the surface, and reusability if it is in powder form [8]. This limits the application of TiO$_2$ in the visible light region, affects photocatalytic efficiency, and slows

down commercialization. Researchers proposed many methods to solve these problems: heterojunction formation [9], doping [10], noble metal deposition, inorganic acids modification, dye sensitization, or metal ion implantation [11]. For example, an increase in photocatalytic efficiency was observed when TiO_2 thin films were doped with a low amount of Cu (0.6 wt.%; k_{Cu} = 0.022 min^{-1}), followed by Mg (0.9 wt.%; k_{Mg} = 0.019 min^{-1}) and Ni (0.5 wt.%; k_{Ni} = 0.013 min^{-1}) [8]. The metal nanoparticles/semiconductor heterojunctions also have great potential in high-performance photocatalysis (plasmonic photocatalysis) [12]. The benefits of metal nanoparticles/semiconductor heterojunctions emerge via metal-semiconductor junction and localized surface plasmon resonance (LSPR). The metal/semiconductor junction extends the e^- and h^+ separation time and increases the charge transfer rate. The LSPR enhances visible light response, UV light absorption, local heating effect, and reduces $e-$ and h^+ diffusion length, etc. [13]. Different effects can be obtained depending on the wavelength of the light. [13,14]. After UV light irradiation, only the semiconductor is excited. Metal nanoparticles act as sinks for photo-induced electrons due to the Schottky barrier [15]. It prolongs the lifespan of photoelectrons, i.e., slows down the recombination process [16]. After VIS light irradiation, LSPR occurs. Three outcomes are possible for LSPR: photon scattering, plasmon resonance energy transfer, and hot electron transfer [14]. These processes increase charge carrier concentration or, in other words, photocatalytic efficiency. After UV-VIS light irradiation, a synergetic effect of UV and VIS light occurs [17].

Thin films technology could solve the reusability problems. Thin films of the desired material are deposited in various ways: spin coating [18], chemical vapor deposition (*CVD*) [19], e-beam evaporation, magnetron sputtering [20], etc. The magnetron sputtering technique has advantages against chemical methods such as controllable structure, stoichiometry, and thickness, good adhesion, homogeneity, low concentration of impurities, etc. The properties of thin films can be controlled by changing sputtering power, gas pressure, the ratio between oxygen and argon, the distance between sample and target, or even the deposition angle [21–25]. The nanoparticles can also be formed using various techniques, but solid-state dewetting is the simplest and probably cheapest method [26]. Pre-existing defects, such as holes, grain boundaries, and thin-film edges, are common in thin films. When such metallic thin films are heated to high enough temperatures, they often dewet the substrate and form isolated islands. The flat films start to form a rim at the grain boundaries, the edges of the film, or other defects. The mass diffuses from the triple point of grain boundaries (or from the defect site) to the flat film resulting in a rim on the surface [27]. The holes expand and develop a thickened surface around them (edge retraction) due to the local curvature gradient at their edges. The net curvature decreases as the rim gets thicker, and edge retraction slows down. The result is a thick rim and valley behind it [28]. From this moment, two outcomes, pinch-off and fingering instability, are possible [29]. The rim cuts off the rest of the mass during the pinch-off process. On the other hand, the rim starts to form finger-like structures of the film during the fingering process if coalescence of the holes occurs. The last part of this evolution is Rayleigh instability, which causes the fingers or wire-like structures to decompose into nanoparticles [30]. The kinetics of the dewetting process and the properties of nanoparticles mainly depend on the temperature, annealing time, and thickness of thin films.

The aim of this paper is to evaluate photocatalytic efficiency by investigating the photodegradation of Rhodamine B aqueous solution under UV light using prepared $AgNP/TiO_2$ structures as photocatalysts. For this reason, AgNPs were formed on the surface of TiO_2 thin films using the solid state dewetting technique. Later, the size, distribution, structure, and photocatalytic activity of AgNPs on TiO_2 thin films were analyzed.

2. Materials and Methods

2.1. The Preparation of TiO₂ Thin Films

TiO_2 thin films (h_{TiO2} = 100 nm) were deposited on glass substrates using a reactive magnetron sputtering technique (PVD-75 Kurt J. Lesker). Before the deposition, a high vac-

uum (up to 4×10^{-3} Pa) was reached using a dual-stage rotary vane and turbo-molecular pumps. Then, the chamber was filled with Ar and O_2 gases (99.999% purity) with a ratio of 20% and 80%, respectively, while ~1.87 Pa pressure was reached. Two Ti targets (99.995% purity) with a diameter of 50.8 mm were used for the deposition. A 1.6 nm/min growth rate using a DC power supply at 250 W sputtering power was achieved.

2.2. Formation of Ag Nanoparticles on the TiO₂ Surface

The Ag thin films (h_{Ag} = 5; 7.5; 10 nm) were deposited on the surface of TiO_2 (Ag/TiO_2) by using a magnetron sputtering technique. After creating a high vacuum (up to 4×10^{-3} Pa), the chamber was filled with a high purity Ar gas until a working pressure of ~2.4 Pa was reached. One Ag target (99.995% purity) with a diameter of 50.8 mm was used for the deposition of Ag thin films. A growth rate of 2.5 nm/min for Ag thin films was reached using a DC power supply at 31 W sputtering power. AgNPs on the TiO_2 surface (AgNP/TiO_2) were formed using the solid-state dewetting (*SSD*) process. Thus, Ag/TiO_2 structures were annealed immediately after deposition in a vacuum chamber (2.4 Pa Ar gas pressure) at different temperatures (T_a) and times (t_a). Since the formation of AgNPs was carried out in a vacuum, the oxidation of silver nanoparticles should be negligibly low. Furthermore, previous research suggests that the concentration of Ag^{+1} and Ag^{+3} oxidation states were not higher than 17%, even though the calcination was done in a furnace under constant Ar gas flow [31].

2.3. Morphological and Structural Analysis

The crystal structure of deposited TiO_2 thin films was investigated by an X-ray diffractometer (*XRD*) Bruker D8 Discover (Bruker, Billerica, MA, USA) at *2θ* in a range of 20° to 70° (with a 0.01° step) using a Cu Kα (λ = 1.54059 Å) radiation. The peak analysis was carried out by using a "Match!" crystallographic analysis software. The morphology of TiO_2 thin films and AgNP/TiO_2 structures were analyzed by a scanning electron microscope (SEM) Hitachi S-3400N (Hitachi High-Technologies Corporation, Tokyo, Japan). The obtained surface images were analyzed by "ImageJ" software to evaluate the parameters of formed AgNPs. The optical properties of prepared samples were measured by a UV-Vis spectrophotometer USB4000 (Ocean Optics Inc., Rochester, NY, USA) in a range of 250 to 800 nm (with a 0.2 nm step) wavelength, and the spectra were analyzed by "OceanArt" software.

2.4. Photocatalytic Efficiency Evaluation

The photocatalytic efficiency was evaluated by the photodegradation of RhB (rhodamine B) (10^{-5} Mol/L) solution under UV-C (254 nm) light irradiation. The samples were immersed in the beaker with 50 mL of RhB solution and placed on the magnetic stirrer under the UV-C light irradiation. Additionally, oxygen gas was introduced into the solution during the measurements, with a 3.6 L/h flow rate, to slightly enhance the photodegradation of RhB. The measurements were conducted in the following order. First, the setup was left in the dark for 30 min to reach the equilibrium between the photocatalyst and RhB solution. Then, the specimen of ~3 mL of RhB was taken, and the light absorbance was measured (which corresponds to the C_0). The subsequent measurements were taken under UV-C irradiation every 20 min. The obtained absorbance values corresponded to C_1, C_2, C_3, etc. The taken RhB solution was returned to the beaker after each measurement. The light absorbance was measured by a UV-Vis spectrophotometer USB4000 (Ocean Optics Inc., Rochester, NY, USA) in the 500 nm–600 nm range, and the spectra were analyzed using the "OceanArt" software. The degradation rate constant (k) was calculated using this formula [32]:

$$k = -\frac{ln\left(\frac{C_i}{C_0}\right)}{t}, \tag{1}$$

where C_0 is initial concentration of RhB, and C_i is concentration of RhB at time t.

While the degradation efficiency D_{efi} was calculated using the formula [33]:

$$D_{efi} = \frac{C_0 + C_i}{C_0} \cdot 100\%, \tag{2}$$

3. Results and Discussion

3.1. The Synthesis of the AgNP/TiO$_2$ Structures

The kinetics of the SSD process depend mainly on the three factors: annealing temperature, annealing time, and initial thickness of thin films [34]. Thus, the mentioned dependencies were analyzed. The Ag thin films with an initial thickness of 10 nm were deposited on the TiO$_2$ surface and annealed at different temperatures (T_a): 300, 350, 400, and 450 °C for 60 min to observe the SSD dependence on the annealing temperature. The highest circularity of AgNPs was 0.918 (0—line, 1—perfect circle) for Ag/TiO$_2$ structures annealed at 400 °C, according to the analysis of the surface images of AgNP/TiO$_2$ (Figure 1). The coverage area and average diameter were 23.18% and 81.97 nm, respectively. Furthermore, the highest ordering (size distribution and coverage) of AgNPs was observed for Ag thin films annealed at 400 °C. Thus, the optimal annealing temperature for Ag thin films with an initial thickness of 10 nm is 400 °C. Furthermore, Serrano et al. found that thicker Ag thin films require higher annealing temperatures for the complete transition from thin films to nanoparticles through the dewetting process [35]. Based on their study, the highest ordering was achieved when Ag thin films of 10 nm thickness were annealed at 400 °C, while further increase in temperature resulted in agglomeration of nanoparticles to larger 3D structures.
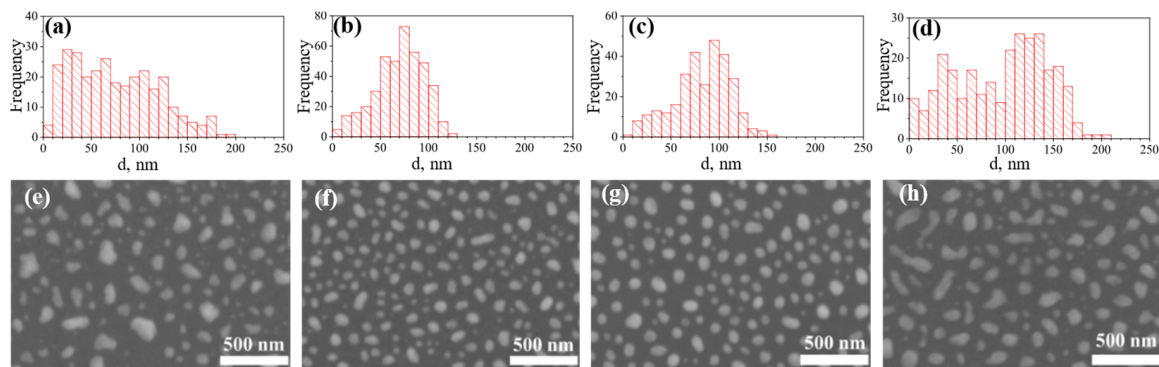

Figure 1. The diameter (*d*) distribution of AgNPs on the TiO$_2$ surface and SEM images of AgNP/TiO$_2$ structures obtained by SSD process (t_a = 60 min, h_{Ag} = 10 nm) at different T_a: (**a**,**e**) 300 °C; (**b**,**f**) 350 °C; (**c**,**g**) 400 °C; (**d**,**h**) 450 °C.

Further analysis of AgNPs formation was done by annealing the Ag thin films of 10 nm thickness at 400 °C using different annealing times, i.e., 10, 20, 40, and 60 min. (Figure 2). After 10 min of annealing, the fractal-like structure was observed. This is the result of the fingering process [36]. The Ag thin films dewetted into smaller AgNPs with an average diameter of ~53.38 nm, when increasing the annealing time to 40 min. After 60 min of annealing, AgNPs agglomerated into bigger islands with an increased average diameter of ~81.97 nm. Therefore, 60 min of annealing time was considered optimal for the evenly distributed formation of AgNPs.

Given these results, further analysis was done with AgNPs obtained by annealing Ag/TiO$_2$ structures with initial Ag thin film thickness of 5, 7.5, and 10 nm at 400 °C temperature for 60 min. The results were AgNP/TiO$_2$ structures where the average diameters of AgNPs were 27, 38, and 82 nm, respectively (Figure 3 and Table 1). The surface resistance of the deposited Ag thin films was measured, resulting in the sheet resistance of 16.96 kΩ for Ag thin films with a thickness of 10 nm. Thus, the Ag thin film was continuous, whereas Ag thin films with a thickness of 5 and 7.5 nm exhibited an insulating behavior, suggesting

that thinner Ag thin films were discontinuous. It agrees with the Huang et al. study, where the sheet resistance drastically increases with a thickness lower than 8 nm for Ag thin films [37]. Moreover, these findings explain the size dependence of AgNPs on the initial thickness of Ag thin films. It is known that the number of holes is inversely proportional to the thickness of continuous films, whereas discontinuous thin films have holes naturally, and the lower number of holes in thicker films results in the formation of enlarged AgNPs.
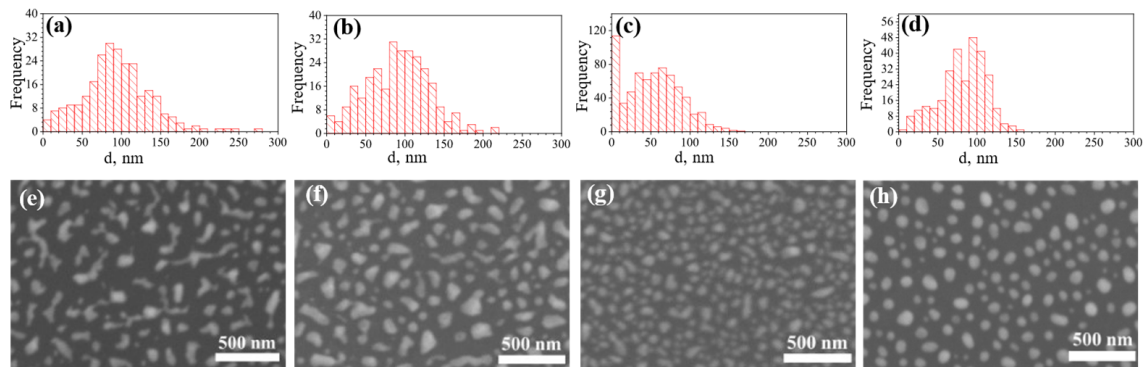
Figure 2. The diameter (*d*) distribution of AgNPs and SEM images of AgNP/TiO$_2$ structures obtained by SSD process (T_a = 400 °C, h_{Ag} = 10 nm) using different t_a: (**a**,**e**) 10 min; (**b**,**f**) 20 min; (**c**,**g**) 40 min; (**d**,**h**) 60 min.
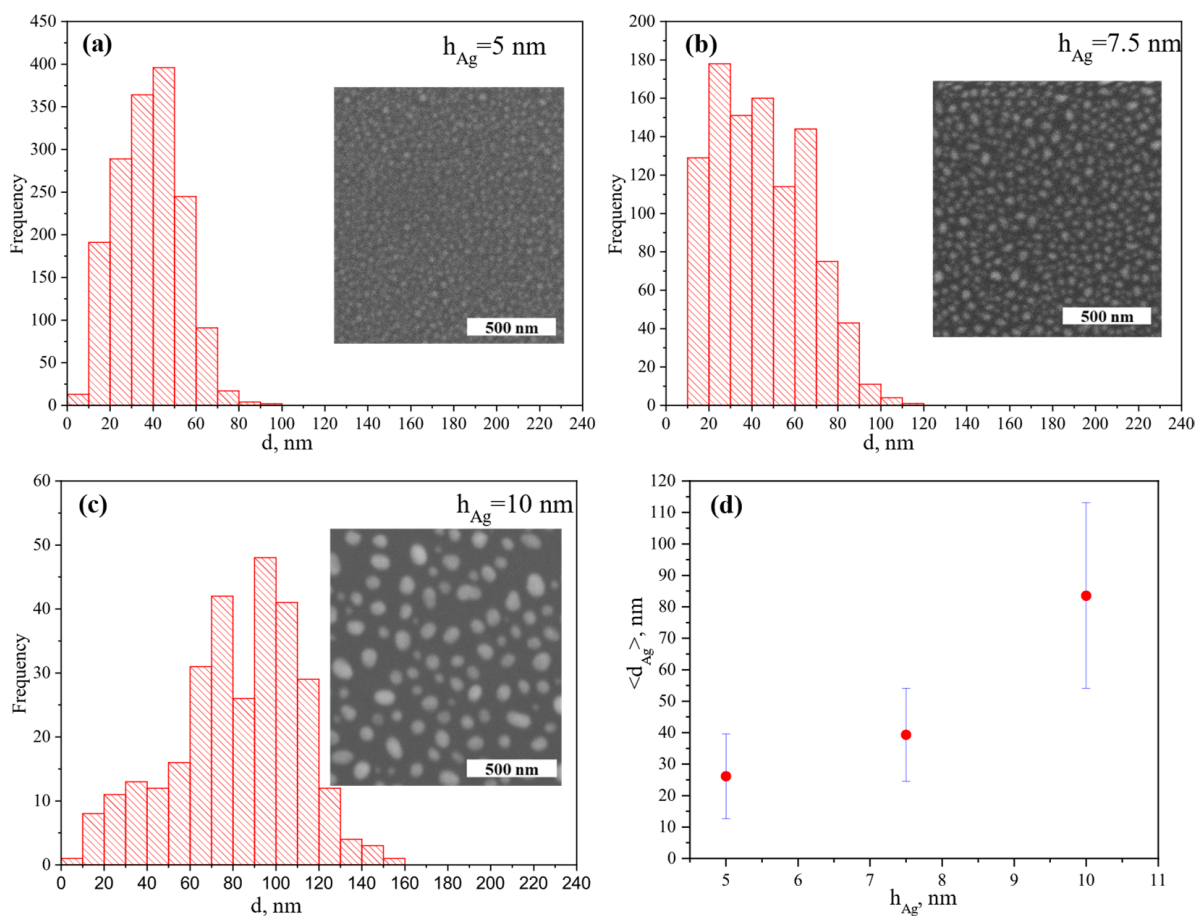

Figure 3. The diameter (*d*) distribution of AgNPs and SEM of AgNP/TiO$_2$ structures obtained by SSD process (T_a = 400 °C, t_a = 60 min) using different h_{Ag}: (**a**) 5 nm; (**b**) 7.5 nm; (**c**) 10 nm, and (**d**) the average NP diameter (**d**) dependence on h_{Ag}.

Table 1. The parameters of AgNPs on the surface of TiO_2.

The Initial Thickness of Ag Thin Films (h_{Ag})	5 nm	7.5 nm	10 nm
Average area (A), nm^2	705	1324	6003
Average diameter (D_A), nm	27	38	82
Density (n), μm^{-2}	398	229	42
Coverage (SC), %	28	30	23

The as-deposited TiO_2 and Ag/TiO_2 did not show any particular peaks (Figure 4) that are attributed to the crystal phase of TiO_2, except the Ag/TiO_2 (with initial Ag thin film thickness of 10 nm) showing the corresponding peak of Ag{111} facet at 38.16° [38]. However, after the SSD process, peaks corresponding to the TiO_2 anatase phase appeared at 25.43°, 38.17°, 48.18°, 54.04°, and 55.15°, with an Ag peak at 44.44° [38–40]. It suggests that the amorphous-to-anatase TiO_2 phase transition occurred during the annealing process, which might positively affect the photocatalytic efficiency of prepared structures [41].
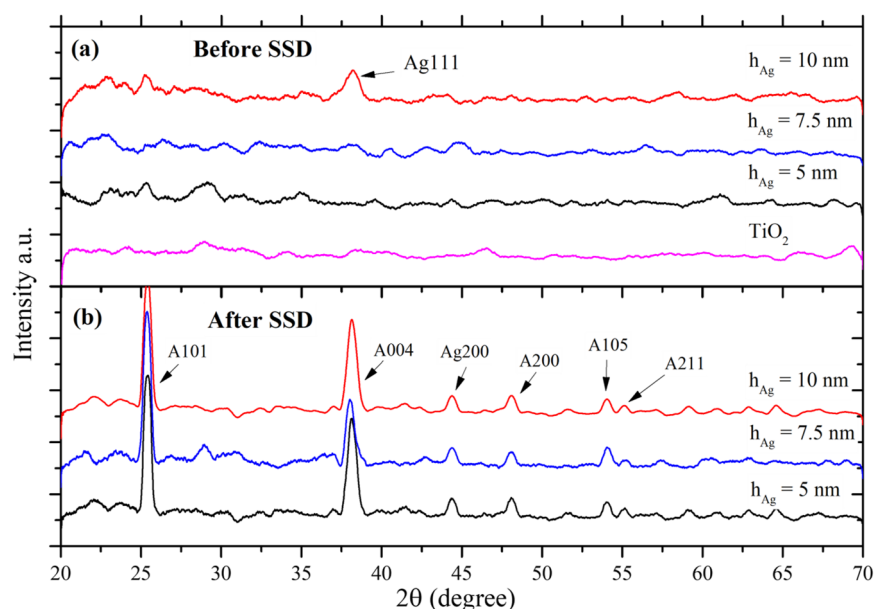
Figure 4. XRD of (**a**) Ag/TiO_2 structures (before SSD) and (**b**) $AgNP/TiO_2$ structures (after SSD).

3.2. Photocatalytic Efficiency

The evaluation of photocatalytic efficiency for prepared $AgNP/TiO_2$ was done by the photodegradation of RhB solution under UV-C light irradiation. The RhB solution has the highest light absorbance at ~550–560 nm wavelength. Thus, this range was taken during the analysis. The light absorbance at 0 min attributes to the initial concentration of RhB (C_0/C_0), and the latter light absorbance attributes to the decrease in concentration after 20, 40, 60, and 80 min and is considered as C_1/C_0, C_2/C_0, C_3/C_0, C_4/C_0 respectively. The 50% decolorization of RhB was reached in ~50 min for $AgNP/TiO_2$, where an average AgNPs diameter was ~38 nm (Figure 6a), whereas the 50% decolorization of RhB by using the $AgNP/TiO_2$ with an average AgNPs diameter of 27 and 82 nm was reached in ~59 min and 58 min, respectively. Considering the TiO_2 as a stand-alone photocatalyst, the same result was reached after ~78 min, and for RhB (without the photocatalyst) only after 100 min.

The LSPR effect can be observed in the transmittance spectra of $AgNP/TiO_2$ structures (Figure 5). The transmittance of visible light reached minimum values in the 550–650 nm range. It can be seen that the LSPR effect increased with the size of AgNPs on the surface of TiO_2 thin films.
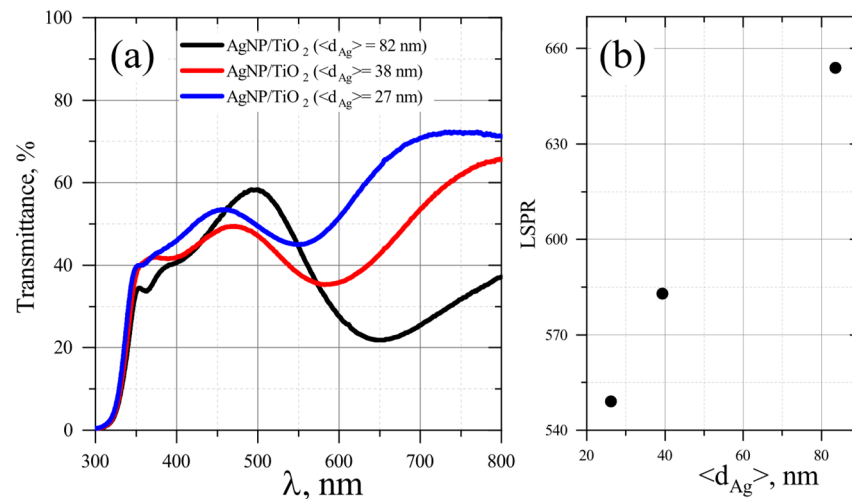
Figure 5. (**a**) Transmittance spectra of AgNP/TiO$_2$ structures and (**b**) LSPR dependency on $<d_{Ag}>$.

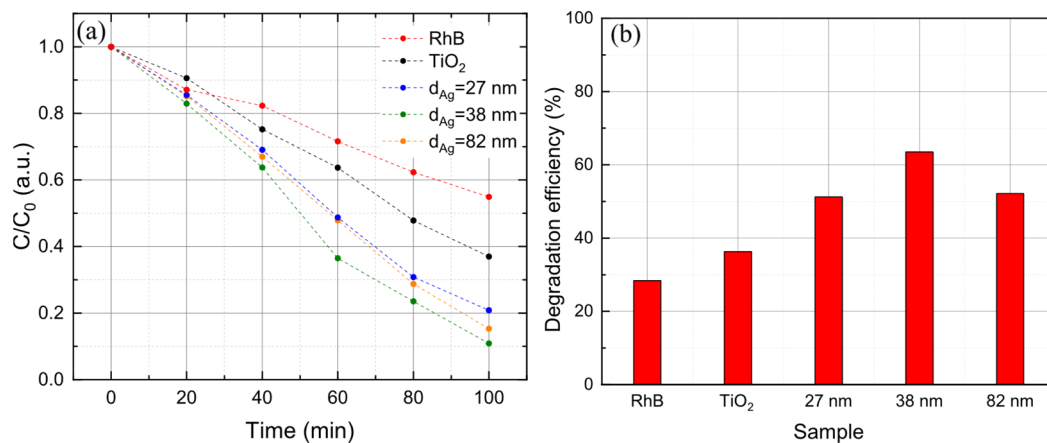**Figure 6.** The photodegradation of RhB under UV-C light irradiation by using an AgNP/TiO$_2$ as a photocatalyst with different NP parameters. (**a**) the kinetics of the photodegradation process and (**b**) the degradation efficiency (D_{efi}) of RhB after 60 min of irradiation.

The degradation efficiency was evaluated after 60 min of UV light irradiation (Figure 6b). Clear dependence between AgNPs diameter and degradation efficiency was not observed. The peak value of photocatalytic efficiency was found for AgNP/TiO$_2$, where an average AgNPs diameter was ~38 nm ($k_{38} = 0.017$ min^{-1}, $D_{efi\_38} = 63.5\%$), whereas degradation rate constant and degradation efficiency for AgNPs of $<d_{Ag}> = 27$ nm and $<d_{Ag}> = 82$ nm were $k_{27} = 0.012$ min^{-1}, $D_{efi\_27} = 51.2\%$ and $k_{82} = 0.011$ min^{-1}, $D_{efi\_82} = 52.1\%$, respectively. It was also found that photocatalytic efficiency of AgNP/TiO$_2$, where $<d_{Ag}> = 38$ nm ($k_{38} = 0.017$ min^{-1}, $D_{efi\_38} = 63.5\%$) was 1.7 times higher than photocatalytic efficiency of pure TiO$_2$ thin films ($k_{TiO2} = 0.008$ min^{-1}, $D_{efi\_TiO2} = 36.3\%$).

Comparison of the results with the literature is complicated due to different experimental conditions, i.e., different initial concentrations of RhB, different active areas of photocatalysts, different light sources, irradiance, etc. Therefore, the results obtained by other authors are contradictory. For example, the 50% decolorization of RhB was reached after ~30 min for anatase thin films by Wang et al. and for TiO$_2$/β-SiC foam by Alle et al., while Wannapop et al. reached 50% decolorization of RhB for TiO$_2$ nanorods only after 4 h [42–44]. Nevertheless, our results suggest that AgNPs can enhance the photocatalytic efficiency of TiO$_2$ thin films. In addition, they are similar to Vezirogl et. al. results [45]. Authors also found that TiO$_2$ thin films decorated with AgNPs (<50 nm) have 1.7 times higher photocatalytic efficiency than bare TiO$_2$ thin films.

The photodegradation of RhB using a photocatalyst consists of a series of chemical reactions (Figure 7): the oxidation reaction on the surface of TiO_2 with a photogenerated hole–H_2O, $OH^- \rightarrow OH$; the reduction reactions on the surface of AgNPs with a photogenerated electron–$O_2 \rightarrow O_2^-$; followed by the degradation of RhB solution itself–$H^+ \rightarrow \cdot HO_2^- / \cdot OH$ and $\cdot HO_2^- \rightarrow CO_2$, H_2O, NO_x, etc. The oxidation and reduction reactions occur on the surface of TiO_2 (Figure 7a), considering the photodegradation of an aqueous solution of RhB using TiO_2 as a photocatalyst. To this matter, there is a higher probability of charge carrier recombination.
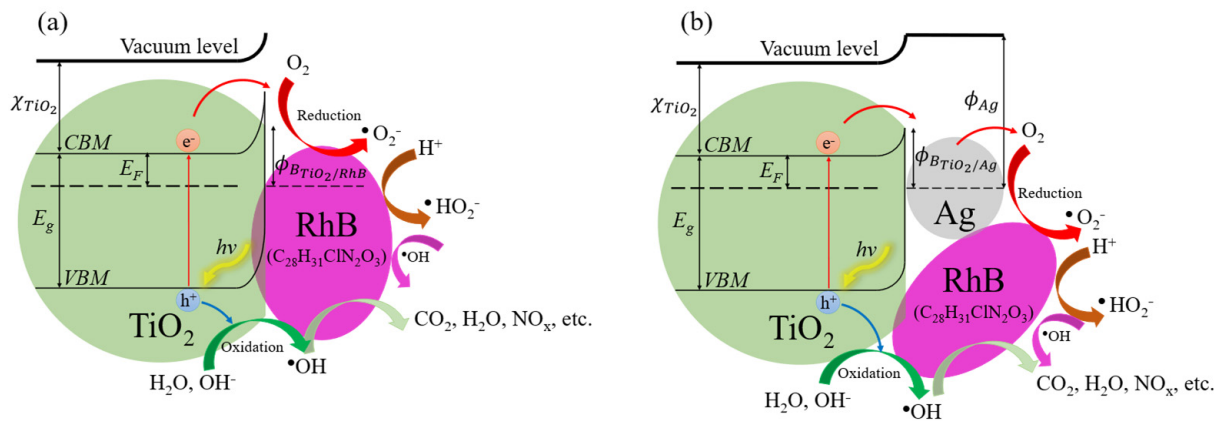

Figure 7. The photodegradation of RhB in an aqueous solution using TiO_2 (**a**) and AgNP/TiO_2 (**b**) as a photocatalyst. *CBM*—conduction band minimum; *VBM*—valence band maximum; E_g—energy band gap; E_F—Fermi energy level; χ_{TiO_2}—electron affinity; $h\nu$—photon energy; e^-—electron; h^+—hole.

AgNPs usually act as electron scavengers [46]. It means that the photogenerated electron is captured (trapped) in AgNPs, where a reduction reaction occurs, and photogenerated holes in TiO_2 take place in the oxidation reaction (Figure 7b) [47–50]. Thus, small and densely packed AgNPs on the surface of TiO_2 should increase the probability of charge carrier separation resulting in higher photocatalytic efficiency. However, such behavior was not observed in the experiments. It can be explained by excessive AgNPs amount on the TiO_2 surface [46]. Very densely packed AgNPs (D_A = 27 nm, n = 398 μm^{-2}) might decrease the photocatalytic activity due to the blocking effect of incoming UV light to the TiO_2 surface, which leads to the decreased generation of electrons. Moreover, very densely packed AgNPs might serve as recombination sites. On the other hand, a low number of trapping sites could be created if the density of AgNPs is low (D_A = 82 nm, n = 42 μm^{-2}).

4. Conclusions

The AgNPs formation and investigation to enhance the photocatalytic efficiency of TiO_2 thin films were investigated in this study. The highest circularity of 0.918 of AgNPs was observed after annealing the Ag/TiO_2 at 400 °C. This study suggests that an optimal annealing time of 60 min is required to get the highest possible distribution of AgNPs when annealing Ag films of 10 nm. A shorter annealing process results in fractal-like structures. Moreover, the analysis of AgNPs formation dependency on the initial thickness (h_{Ag}) of Ag thin films suggests that thin films with a thickness lower than 10 nm are discontinuous. The results show that the density of AgNPs is inversely proportional to the thickness of Ag thin films: h_{Ag} = 5 nm, D = 398 μm^{-2}; h_{Ag} = 7.5 nm, D = 229 μm^{-2}; h_{Ag} = 10 nm, D_A = 42 μm^{-2}. The photodegradation experiments revealed that the photocatalytic efficiency increases for the AgNP/TiO_2 structure compared to stand-alone TiO_2 (k_{TiO2} = 0.008 min^{-1}; D_{efi_TiO2} = 36.3%). The highest efficiency of D_{efi_38} = 63.5% (k_{38} = 0.017 min^{-1}) was observed for the AgNP/TiO_2, where an average AgNPs diameter was 38 nm, whereas for the AgNPs with D_A = 27 nm—D_{efi_27} = 51.2% (k_{27} = 0.012 min^{-1}) and D_A = 82 nm—D_{efi_82} = 52.1% (k_{82} = 0.011 min^{-1}). The nonlinear dependence of degradation efficiency on AgNPs size could be expanded by AgNPs density variation.

AgNP could block UV light and act as recombination sites when the density of AgNPs is very high, whereas a small number of trapping sites could be created when the density of AgNPs is low.

References

1. Forato, F.; Talebzadeh, S.; Rousseau, N.; Mevellec, J.Y.; Bujoli, B.; Knight, D.A.; Queffélec, C.; Humbert, B. Functionalized core–shell Ag@TiO$_2$ nanoparticles for enhanced Raman spectroscopy: A sensitive detection method for Cu(II) ions. *Phys. Chem. Chem. Phys.* **2019**, *21*, 3066–3072. [CrossRef] [PubMed]

2. Yunus, I.S.; Harwin; Kurniawan, A.; Adityawarman, D.; Indarto, A. Nanotechnologies in water and air pollution treatment. *Environ. Technol. Rev.* **2012**, *1*, 136–148. [CrossRef]

3. Xu, C.; Ravi Anusuyadevi, P.; Aymonier, C.; Luque, R.; Marre, S. Nanostructured materials for photocatalysis. *Chem. Soc. Rev.* **2019**, *48*, 3868–3902. [CrossRef] [PubMed]

4. Li, K.; Lu, X.; Zhang, Y.; Liu, K.; Huang, Y.; Liu, H. Bi$_3$TaO$_7$/Ti$_3$C$_2$ heterojunctions for enhanced photocatalytic removal of water-borne contaminants. *Environ. Res.* **2020**, *185*, 109409. [CrossRef]

5. Huang, Y.; Fan, W.; Long, B.; Li, H.; Zhao, F.; Liu, Z.; Tong, Y.; Ji, H. Visible light Bi$_2$S$_3$/Bi$_2$O$_3$/Bi$_2$O$_2$CO$_3$ photocatalyst for effective degradation of organic pollutions. *Appl. Catal. B Environ.* **2016**, *185*, 68–76. [CrossRef]

6. Nakata, K.; Fujishima, A. TiO$_2$ photocatalysis: Design and applications. *J. Photochem. Photobiol. C Photochem. Rev.* **2012**, *13*, 169–189. [CrossRef]

7. Acedo_Mendoza, A.G.; Infantes-Molina, A.; Vargas-Hernández, D.; Chávez-Sánchez, C.A.; Rodríguez-Castellón, E.; Tánori-Córdova, J.C. Photodegradation of methylene blue and methyl orange with CuO supported on ZnO photocatalysts: The effect of copper loading and reaction temperature. *Mater. Sci. Semicond. Process.* **2020**, *119*, 105257. [CrossRef]

8. Natarajan, T.S.; Thomas, M.; Natarajan, K.; Bajaj, H.C.; Tayade, R.J. Study on UV-LED/TiO$_2$ process for degradation of Rhodamine B dye. *Chem. Eng. J.* **2011**, *169*, 126–134. [CrossRef]

9. Kavaliunas, V.; Hatanaka, Y.; Neo, Y.; Laukaitis, G.; Mimura, H. Structural Design of TiO$_2$ /Si Hybrid Photoelectrode and Pt-Free Counter Photoelectrodes for Charge Carrier Separation in Water-Splitting Reactions. *ECS J. Solid State Sci. Technol.* **2021**, *10*, 103015. [CrossRef]

10. Kavaliunas, V.; Krugly, E.; Sriubas, M.; Mimura, H.; Laukaitis, G.; Hatanaka, Y. Influence of Mg, Cu, and Ni dopants on amorphous TiO$_2$ thin films photocatalytic activity. *Materials* **2020**, *13*, 886. [CrossRef]

11. Singh, S.; Mahalingam, H.; Singh, P.K. Polymer-supported titanium dioxide photocatalysts for environmental remediation: A review. *Appl. Catal. A Gen.* **2013**, *462–463*, 178–195. [CrossRef]

12. Humayun, M.; Raziq, F.; Khan, A.; Luo, W.; Luo, W. Modification strategies of TiO$_2$ for potential applications in photocatalysis: A critical review. *Green Chem. Lett. Rev.* **2018**, *11*, 86–102. [CrossRef]

13. Kumar, A.; Choudhary, P.; Kumar, A.; Camargo, P.H.C.; Krishnan, V. Recent Advances in Plasmonic Photocatalysis Based on TiO$_2$ and Noble Metal Nanoparticles for Energy Conversion, Environmental Remediation, and Organic Synthesis. *Small* **2022**, *18*, 2101638. [CrossRef] [PubMed]

14. Wakeford, R.; Chun-Che Lin, L.; Hu, C.P.; Takata, J.; Zhang, X.; Lim Chen, Y.; Liu, R.S.; Ping Tsai, D. Plasmonic photocatalysis. *Rep. Prog. Phys.* **2013**, *76*, 046401.

15. Khan, M.R.; Chuan, T.W.; Yousuf, A.; Chowdhury, M.N.K.; Cheng, C.K. Schottky barrier and surface plasmonic resonance phenomena towards the photocatalytic reaction: Study of their mechanisms to enhance the photocatalytic activity. *Catal. Sci. Technol.* **2015**, *5*, 2522–2531. [CrossRef]

16. Permporn, D.; Khunphonoi, R.; Wilamat, J.; Khemthong, P.; Chirawatkul, P.; Butburee, T.; Sangkhun, W.; Wantala, K.; Grisdanurak, N.; Santatiwongchai, J.; et al. Insight into the Roles of Metal Loading on CO_2 Photocatalytic Reduction Behaviors of TiO_2. *Nanomaterials* **2022**, *12*, 474. [CrossRef]

17. Kowalska, E.; Remita, H.; Colbeau-Justin, C.; Hupka, J.; Belloni, J. Modification of Titanium Dioxide with Platinum Ions and Clusters: Application in Photocatalysis. *J. Phys. Chem. C* **2008**, *112*, 1124–1131. [CrossRef]

18. Zhang, H.; Itoi, T.; Konishi, T.; Izumi, Y. Dual Photocatalytic Roles of Light: Charge Separation at the Band Gap and Heat via Localized Surface Plasmon Resonance to Convert CO_2 into CO over Silver-Zirconium Oxide. *J. Am. Chem. Soc.* **2019**, *141*, 6292–6301. [CrossRef]

19. Khan, M.I.; Bhatti, K.A.; Qindeel, R.; Althobaiti, H.S.; Alonizan, N. Structural, electrical and optical properties of multilayer TiO_2 thin films deposited by sol–gel spin coating. *Results Phys.* **2017**, *7*, 1437–1439. [CrossRef]

20. Aghaee, M.; Verheyen, J.; Stevens, A.A.E.; Kessels, W.M.M.; Creatore, M. TiO_2 thin film patterns prepared by chemical vapor deposition and atomic layer deposition using an atmospheric pressure microplasma printer. *Plasma Process. Polym.* **2019**, *16*, 1900127. [CrossRef]

21. Wang, Y.H.; Rahman, K.H.; Wu, C.C.; Chen, K.C. A Review on the Pathways of the Improved Structural Characteristics and Photocatalytic Performance of Titanium Dioxide (TiO_2) Thin Films Fabricated by the Magnetron-Sputtering Technique. *Catalysts* **2020**, *10*, 598. [CrossRef]

22. Hoskins, B.D.; Strukov, D.B. Maximizing stoichiometry control in reactive sputter deposition of TiO_2. *J. Vac. Sci. Technol. A Vac. Surf. Film.* **2017**, *35*, 020606. [CrossRef]

23. Vrakatseli, V.; Farsari, E.; Mataras, D. Wetting Properties of Transparent Anatase/Rutile Mixed Phase Glancing Angle Magnetron Sputtered Nano-TiO_2 Films. *Micromachines* **2020**, *11*, 616. [CrossRef] [PubMed]

24. Toku, H.; Pessoa, R.S.; Maciel, H.S.; Massi, M.; Mengui, U.A. Influence of process parameters on the growth of pure-phase anatase and rutile TiO_2 thin films deposited by low temperature reactive magnetron sputtering. *Braz. J. Phys.* **2010**, *40*, 340–343. [CrossRef]

25. Yang, W.J.; Hsu, C.Y.; Liu, Y.W.; Hsu, R.Q.; Lu, T.W.; Hu, C.C. The structure and photocatalytic activity of TiO_2 thin films deposited by dc magnetron sputtering. *Superlattices Microstruct.* **2012**, *52*, 1131–1142. [CrossRef]

26. Musil, J.; Heřman, D.; Šícha, J. Low-temperature sputtering of crystalline TiO_2 films. *J. Vac. Sci. Technol. A Vac. Surf. Film.* **2006**, *24*, 521. [CrossRef]

27. Thompson, C.V. Solid-State Dewetting of Thin Films. *Annu. Rev. Mater. Res.* **2012**, *42*, 399–434. [CrossRef]

28. Jiran, E.; Thompson, C.V. Capillary instabilities in thin films. *J. Electron. Mater.* **1990**, *19*, 1153–1160. [CrossRef]

29. Hyun Kim, G.; Zucker, R.V.; Ye, J.; Craig Carter, W.; Thompson, C.V. Quantitative analysis of anisotropic edge retraction by solid-state dewetting of thin single crystal films. *J. Appl. Phys.* **2013**, *113*, 043512. [CrossRef]

30. Ye, J.; Zuev, D.; Makarov, S. Dewetting mechanisms and their exploitation for the large-scale fabrication of advanced nanophotonic systems. *Int. Mater. Rev.* **2019**, *64*, 439–477. [CrossRef]

31. Sriubas, M.; Bockute, K.; Palevicius, P.; Kaminskas, M.; Rinkevicius, Z.; Ragulskis, M.; Simonyte, S.; Ruzauskas, M.; Laukaitis, G. Antibacterial Activity of Silver and Gold Particles Formed on Titania Thin Films. *Nanomaterials* **2022**, *12*, 1190. [CrossRef] [PubMed]

32. Rezaei, M.; Habibi-Yangjeh, A. Simple and large scale refluxing method for preparation of Ce-doped ZnO nanostructures as highly efficient photocatalyst. *Appl. Surf. Sci.* **2013**, *265*, 591–596. [CrossRef]

33. Karimi, L.; Zohoori, S.; Yazdanshenas, M.E. Photocatalytic degradation of azo dyes in aqueous solutions under UV irradiation using nano-strontium titanate as the nanophotocatalyst. *J. Saudi Chem. Soc.* **2014**, *18*, 581–588. [CrossRef]

34. Xu, S.; Li, P.; Lu, Y. In situ atomic-scale analysis of Rayleigh instability in ultrathin gold nanowires. *Nano Res.* **2017**, *11*, 625–632. [CrossRef]

35. Leroy, F.; Borowik, L.; Cheynis, F.; Almadori, Y.; Curiotto, S.; Trautmann, M.; Barbé, J.C.; Müller, P. How to control solid state dewetting: A short review. *Surf. Sci. Rep.* **2016**, *71*, 391–409. [CrossRef]

36. Serrano, A.; Llorca-Hernando, O.; Del Campo, A.; Rubio-Marcos, F.; Rodríguez de La Fuente, O.; Fernández, J.F.; García, M.A. Ag-AgO nanostructures on glass substrates by solid-state dewetting: From extended to localized surface plasmons. *J. Appl. Phys.* **2018**, *124*, 133103. [CrossRef]

37. McCallum, M.S.; Voorhees, P.W.; Miksis, M.J.; Davis, S.H.; Wong, H. Capillary instabilities in solid thin films: Lines. *J. Appl. Phys.* **1996**, *79*, 7604–7611. [CrossRef]

38. Huang, J.; Liu, X.; Lu, Y.; Zhou, Y.; Xu, J.; Li, J.; Wang, H.; Fang, J.; Yang, Y.; Wang, W.; et al. Seed-layer-free growth of ultra-thin Ag transparent conductive films imparts flexibility to polymer solar cells. *Sol. Energy Mater. Sol. Cells* **2018**, *184*, 73–81. [CrossRef]

39. Meng, Y. A sustainable approach to fabricating ag nanoparticles/PVA hybrid nanofiber and its catalytic activity. *Nanomaterials* **2015**, *5*, 1124–1135. [CrossRef]

40. Bensouici, F.; Bououdina, M.; Dakhel, A.A.; Tala-Ighil, R.; Tounane, M.; Iratni, A.; Souier, T.; Liu, S.; Cai, W. Optical, structural and photocatalysis properties of Cu-doped TiO_2 thin films. *Appl. Surf. Sci.* **2017**, *395*, 110–116. [CrossRef]

41. Prasai, B.; Cai, B.; Underwood, M.K.; Lewis, J.P.; Drabold, D.A. Properties of amorphous and crystalline titanium dioxide from first principles. *J. Mater. Sci.* **2012**, *47*, 7515–7521. [CrossRef]

42. Hui, W.; Guodong, S.; Xiaoshu, Z.; Wei, Z.; Lin, H.; Ying, Y. In-situ synthesis of TiO_2 rutile/anatase heterostructure by DC magnetron sputtering at room temperature and thickness effect of outermost rutile layer on photocatalysis. *J. Environ. Sci.* **2017**, *60*, 33–42. [CrossRef] [PubMed]

43. Wannapop, S.; Somdee, A.; Bovornratanaraks, T. Experimental study of thin film Fe_2O_3/TiO_2 for photocatalytic Rhodamine B degradation. *Inorg. Chem. Commun.* **2021**, *128*, 108585. [CrossRef]

44. Allé, P.H.; Fanou, G.D.; Robert, D.; Adouby, K.; Drogui, P. Photocatalytic degradation of Rhodamine B dye with TiO_2 immobilized on SiC foam using full factorial design. *Appl. Water Sci.* **2020**, *10*, 207. [CrossRef]

45. Veziroglu, S.; Ghori, M.Z.; Obermann, A.L.; Röder, K.; Polonskyi, O.; Strunskus, T.; Faupel, F.; Aktas, O.C. Ag Nanoparticles Decorated TiO2 Thin Films with Enhanced Photocatalytic Activity. *Phys. Status Solidi.* **2019**, *216*, 1800898. [CrossRef]

46. Li, J.; Xu, J.; Dai, W.L.; Fan, K. Dependence of Ag Deposition Methods on the Photocatalytic Activity and Surface State of TiO_2 with Twistlike Helix Structure. *J. Phys. Chem.* **2009**, *113*, 8343–8349. [CrossRef]

47. Khore, S.K.; Kadam, S.R.; Naik, S.D.; Kale, B.B.; Sonawane, R.S. Solar light active plasmonic Au@TiO_2 nanocomposite with superior photocatalytic performance for H_2 production and pollutant degradation. *New J. Chem. C* **2018**, *42*, 10958–10968. [CrossRef]

48. Yang, W.; Shen, H.; Min, H.; Ge, J. Enhanced visible light-driven photodegradation of rhodamine B by Ti^{3+} self-doped TiO_2@Ag nanoparticles prepared using Ti vapor annealing. *J. Mater. Sci.* **2020**, *55*, 701–712. [CrossRef]

49. Paul, K.K.; Giri, P.K. Role of Surface Plasmons and Hot Electrons on the Multi-Step Photocatalytic Decay by Defect Enriched Ag@TiO_2 Nanorods under Visible Light. *J. Phys. Chem. C* **2017**, *121*, 20016–20030. [CrossRef]

50. Khalid, N.R.; Mazia, U.; Tahir, M.B.; Niaz, N.A.; Javid, M.A. Photocatalytic degradation of RhB from an aqueous solution using Ag_3PO_4/N-TiO_2 heterostructure. *J. Mol. Liq.* **2020**, *313*, 113522. [CrossRef]